Article

The Effect of Grinding Wheel Contact Stiffness on Plunge Grinding Cycle

Fukuo Hashimoto [1,*] and **Hiroto Iwashita [2]**

[1] Advanced Finishing Technology Ltd., Akron, OH 44319, USA
[2] Toba Engineering, Saku, Nagano 384-2101, Japan; toba108108@gmail.com
*   Correspondence: fukuohashimoto@gmail.com

check for updates

Abstract: This paper presents the effect of grinding wheel contact stiffness on the plunge grinding cycle. First, it proposes a novel model of the generalized plunge grinding system. The model is applicable to all plunge grinding operations including cylindrical, centerless, shoe-centerless, internal, and shoe-internal grinding. The analysis of the model explicitly describes transient behaviors during the ramp infeed and the spark-out in the plunge grinding cycle. Clarification is provided regarding the premise that the system stiffness is composed of machine stiffness and wheel contact stiffness, and these stiffnesses significantly affect productivity and grinding accuracy. The elastic deflection of the grinding wheel is accurately measured and formulas for representing the deflection nature under various contact loads are derived. The deflection model allows us to find the non-linear contact stiffness with respect to the normal load. The contact stiffnesses of four kinds of grinding wheels with different grades and bond materials are presented. Both cylindrical grinding and centerless grinding tests are carried out, and it is experimentally revealed that the time constant at ramp infeed and spark-out is significantly prolonged by reducing the grinding force. It is verified that a simulation of the grinding tests using the proposed model can accurately predict critical parameters like forces and machine deflection during plunge grinding operations. Finally, this paper provides a guideline for grinding cycle design in order to achieve the required productivity and grinding accuracy.

Keywords: grinding; grinding wheel; contact stiffness; plunge grinding; grinding machine

1. Introduction

In the plunge grinding of cylindrical components, the grinding performance is assessed by productivity and grinding accuracy. The productivity in the number of finished parts per unit time is determined by the grinding cycle time consisting of the plunge-infeed time and the spark-out time. As the actual infeed to the CNC command has a time delay, the required cycle time is largely affected by the system stiffness. On the other hand, the grinding accuracy is significantly governed by the system stiffness. In fact, the actual depth of cut always lower than the command value due to the elastic deflections of the grinding system. These deflections become the root cause of geometrical errors such as size error, profile error, roundness error, etc., in the ground products.

The system stiffness is composed of the grinding machine stiffness and the contact stiffness of grinding wheel. The machine stiffness has a linear characteristic under general grinding conditions, and it is relatively easy to integrate it to the grinding system. However, it is well known that the contact deflection in wheel-workpiece interactions shows a non-linear characteristic. As the result, the process parameters like grinding forces in the grinding cycle exhibit complicated behaviors and the phenomena make it difficult to design a proper grinding cycle. Thus, it is crucial to take the influence of contact stiffness on the grinding processes into account in order to achieve the required productivity and accuracy.

There are many publications related to the wheel contact stiffness. However, no published paper has described the effect of wheel contact stiffness on the plunge grinding cycle. Much research has been done in the area of grinding wheel deflection. Hahn [1] first suggested that the deflection of the wheel surface could explain the differences in material removal rates arising from the conformity difference between internal and external grinding. Peklenik [2] proposed the use of the thermocouple method to measure grinding temperature and contact length. He showed a difference in the effective number of cutting points with the wheel grade which attributed to differences in wheel elasticity. Snoeys and Wang [3] carried out static loading tests to verify their model of grain mounted on springs and concluded that the model provided more realistic values for the deflection of the wheel.

Brown, Saito, and Shaw [4] analyzed the influence of elastic deflection on contact length and established a contact length model using Hertzian theory. Kumar and Shaw [5] analyzed the deflection of the grinding wheel and workpiece separately and concluded that the predominant deflection was due to the grinding wheel, not the workpiece. Krug and Honcia [6] estimated the amount of local wheel deflection and found that it would be on the order of 1 μm for a vitrified wheel and 2.5 μm for a resinoid wheel.

Nakayama, Brecker, and Shaw [7] conducted experiments to measure the deflection associated with an individual grain and showed that the local elastic deformation of the grain was the same order of magnitude as the undeformed chip thickness. Nakayama [8] observed deflection of the grains that behaved as if the grains on the wheel were supported by non-linear springs. Zhou and Lutterwelt [9] presented a measuring method to identify the maximum contact length and local length at the wheel-work contact zone. Rowe et al. [10] proposed a model based on the theory of cylinders in contact, including the effect of grains, and explained why measured contact length can be 50% to 200% greater than geometric contact length.

Hucker, Farris, and Chandrasekar [11] conducted grinding tests to measure machine and wheel deflection under various grinding loads and concluded that the contact stiffness of CBN wheels is about three times greater than that of Al_2O_3 wheels. Yamada et al. [12,13] proposed a model of a wheel consisting of rigid body and spring elements and measured the contact stiffness of the wheel under both stationary conditions and grinding operations. Papanikolaou and Salonitis [14] applied a three-dimensional molecular dynamics simulation to investigate the effect of contact stiffness on grinding processes under various grinding speeds.

Self-excited regenerative chatter vibrations are another aspect of the contact stiffness of the wheel that havet been extensively investigated. Chatter vibrations are generally associated with the dynamic compliances of the grinding machine, and a great deal of research has been devoted to understanding these instabilities [15–19]. Snoeys and Brown [20] proposed a model representing work-regenerative and wheel-regenerative chatter vibrations in cylindrical grinding. The model was represented by a block diagram with feedback loops of machine compliances, including the contact stiffness of the wheel.

Inasaki [21] experimentally investigated wheel contact stiffness with hard-spring characteristics and pointed out that it changed with grinding conditions such as speed ratio, depth of cut, etc. He discussed the effects of contact stiffness on the stability of the chatter vibrations. Miyashita, Hashimoto, and Kanai [22] analyzed the dynamic stability of a centerless grinding system and proposed a new setup index for suppressing work-regenerative chatter vibrations. Their model indicated that the contact stiffnesses of both the grinding wheel and regulating wheel had significant influence on chatter vibrations. Hashimoto, Kanai, and Miyashita [23] investigated the growing mechanism of chatter vibrations in cylindrical grinding and proposed a stabilization index related to the wheel contact stiffness for selecting the grinding wheel specifications. A parameter related to the dynamic time constant was introduced and discussed the in-process measurement of the time constant to predict the stability of the chatter vibrations.

In the field of grinding cycle investigations, King and Hahn [24] analyzed a cylindrical grinding system and introduced a concept of time constant which was applicable to the cylindrical grinding, but not to centerless grinding. Malkin and Koren [25] investigated the plunge grinding cycle and proposed

accelerated spark-out to reduce the cycle time. Chiu and Malkin [26] presented a simulation of the grinding parameters specific to infeed cylindrical grinding.

The aforementioned research concentrated primarily on the modeling and measurement of real contact length and the deflection characteristics at the local contact zone of the wheel. This literature revealed the nature of wheel elastic deflection and provided valuable evidence about contact stiffness with hard-spring characteristics. However, the extensive knowledge gleaned about wheel deflection has been little used in practical applications. Current practices for determining the operational grinding conditions of the grinding cycle still largely rely on a cut-and-try method. One reason for this may be the disconnection between the scientific parameters used in past research and the practical parameters required for real-world grinding operations.

It is necessary to establish practical procedures for setting up the proper grinding conditions including grinding stocks, infeed rates, spark-out time, and the selection of the grinding wheel. Furthermore, clear guidelines for designing the grinding cycle that take the effect of contact stiffness on grinding performance into account are indispensable.

This paper presents the effect of grinding wheel contact stiffness on the plunge grinding cycle. It also provides guidelines for the design of the grinding cycle. First, the generalized plunge grinding system including cylindrical, centerless, shoe-centerless, internal, and shoe-internal grinding is explicitly described and analyzed in terms of system outputs corresponding to the inputs of the plunge grinding conditions. The analysis describes the influence of system stiffness on the time constant that governs the transient behaviors of the process parameters such as forces, power, and machine elastic deflection. Additionally, it clarifies that system stiffness is composed of machine stiffness and wheel contact stiffness. These stiffnesses significantly affect the grinding performance indicators such as productivity and grinding accuracy.

The elastic deflection of the grinding wheel is accurately measured and a function for representing the deflection nature under various contact loads is derived. The function allows us to find the non-linear contact stiffness with respect to the normal load. The contact stiffnesses of four kinds of grinding wheels with different grades and bond materials are presented, and the changes in contact stiffness after dressing are discussed.

Experimental tests for both cylindrical grinding and centerless grinding are conducted, and it is experimentally confirmed that the time constant at ramp infeed and spark-out is significantly prolonged by reducing the grinding force. It is verified that a simulation of the grinding tests using the proposed model can accurately predict critical parameters like forces, machine deflection, and system stiffness during plunge grinding operations. Finally, this paper emphasizes that it is vital to take the effect of wheel contact stiffness into consideration during the design of the plunge grinding cycle.

2. Plunge Grinding System and the Grinding Cycle

2.1. Plunge Grinding System

In order to investigate the effect of the grinding wheel's elastic contact deflection on the plunge grinding process, it is necessary to clarify the relationship between the operational setup parameters and the machine characteristics (including the abrasive tools). There are several methods of plunge internal and external grinding, as shown in Figure 1. The grinding method parameter c is used to identify the influence of the amount of infeed on the size reduction of the workpieces. In the centerless grinding and shoe centerless grinding methods (Figure 1d,e), the amount of infeed becomes the diameter reduction of the workpieces and $c = 0.5$ is denoted. On the other hand, in Figure 1a–c,f, the amount of infeed gives the radial reduction on the external or internal ground surface of the workpieces, and $c = 1.0$ is assigned for these methods.
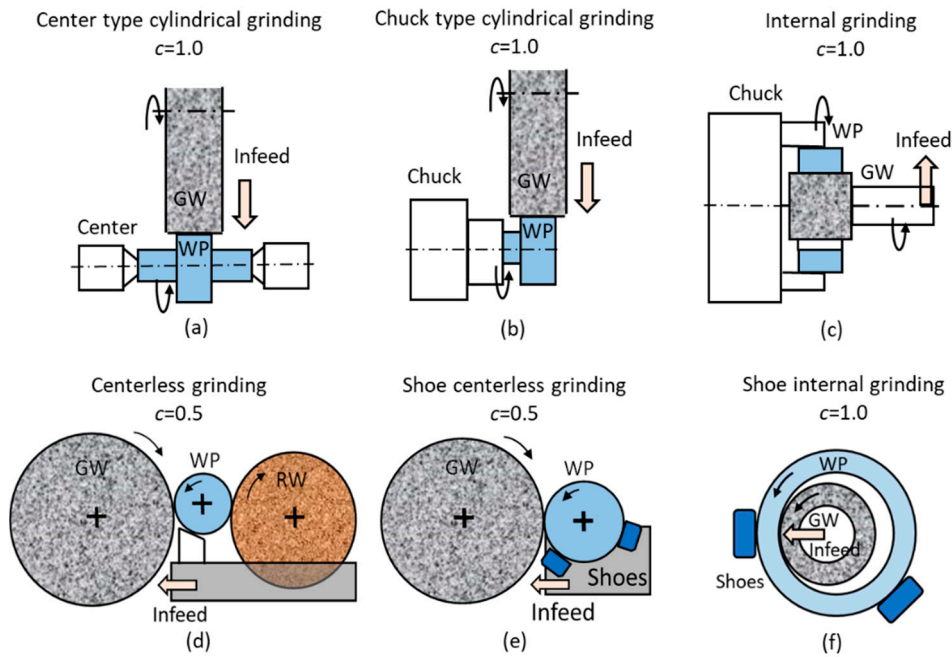
Figure 1. Plunge grinding operations and the method parameter *c*. (**a**) Center type cylindrical grinding; (**b**) Chuck type cylindrical grinding; (**c**) Internal grinding; (**d**) Centerless grinding; (**e**) Shoe centerless grinding; (**f**) Shoe internal grinding.

In plunge grinding, as shown in Figure 1, the grinding wheel mounted on the infeed slide is fed into the workpiece as a command infeed If. The actual infeed r_w can be expressed by:

$$r_w(t) = I_f(t) - d_e(t) \tag{1}$$

where t is the grinding time and d_e is the elastic deflection of the grinding system including the contact deflection of grinding wheel. The actual infeed rate f_i is:

$$f_i(t) = \frac{dr_w(t)}{dt}. \tag{2}$$

The SMRR (specific material removal rate) $Q_w{'}$ is expressed by:

$$Q_w{'}(t) = c \cdot \pi \cdot d_w \cdot f_i(t) \tag{3}$$

where d_w is the internal or external diameter of the workpiece. The MRR (material removal rate) Q_w is:

$$Q_w(t) = b \cdot Q_w{'}(t) \tag{4}$$

where b is the grinding width. The normal grinding force F_n can be written as follows:

$$F_n(t) = \frac{\eta \cdot u}{v_s} \cdot Q_w(t) \tag{5}$$

where η is the force ratio of F_n to tangential force Ft, v_s is the grinding speed, and u is the specific energy. The elastic deflection d_e of the grinding system in the infeed direction can be expressed by:

$$d_e(t) = \frac{1}{k_{eq}} \cdot F_n(t) \tag{6}$$

where k_{eq} is the equivalent system stiffness.

Equivalent system stiffness k_{eq} consists of the stiffness of each machine structure involved in the grinding system and the stiffness of the grinding wheel. The main components of equivalent stiffness k_{eq} are shown in Figure 2. Material removal by grinding generates a normal grinding force F_n, as described in Equation (5). The force F_n gives the elastic deflection d_e, which is determined by the system stiffness k_{eq}. Figure 2a,b illustrate the stiffnesses k_s *and* k_w of the grinding wheel support system and the workpiece support system, respectively. Figure 2c shows the stiffness k_{wo} of workpiece itself, which cannot be ignored when k_{wo} is low (as in the case of thin-wall rings). Figure 2d shows the local deflection δ_c at the contact area between the grinding wheel and the workpiece, and k_c is the contact stiffness of the grinding wheel.
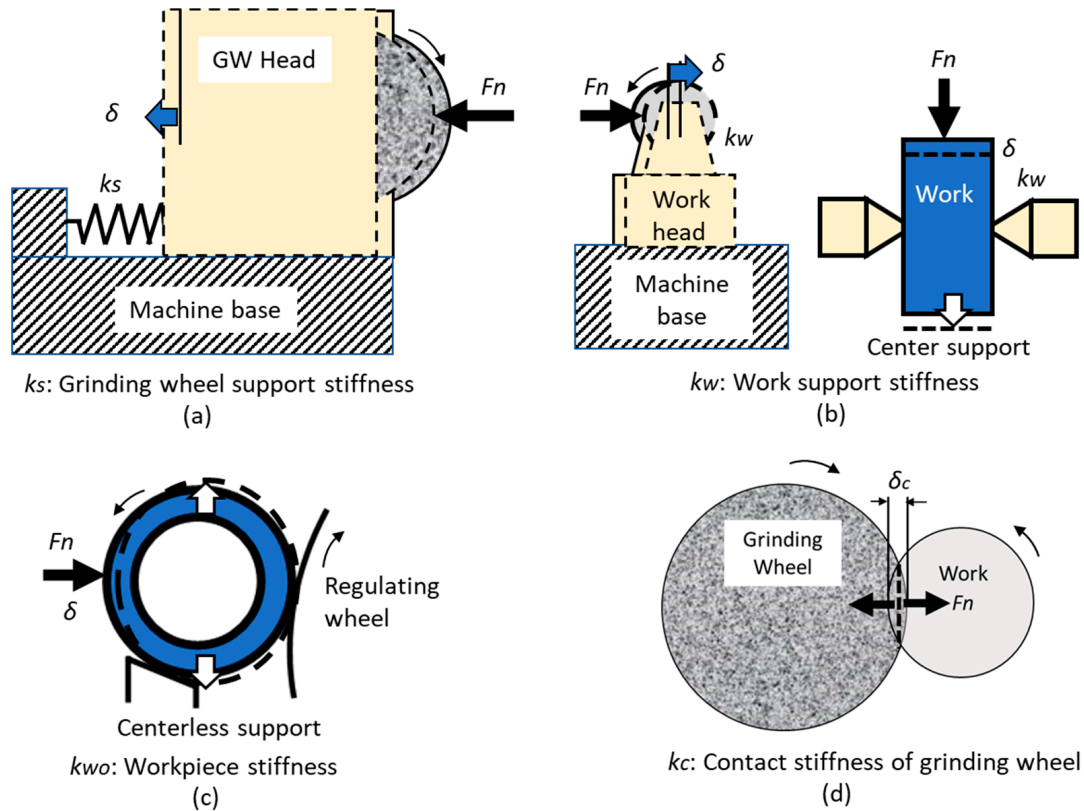

Figure 2. Components of equivalent system stiffness in plunge grinding system. (**a**) Stiffness of grinding wheel head; (**b**) Stiffness of work head; (**c**) Stiffness of workpiece; (**d**) Contact stiffness of grinding wheel.

The equivalent system stiffness k_{eq} is expressed by:

$$\frac{1}{k_{eq}} = \frac{1}{k_m} + \frac{1}{k_c} \tag{7}$$

where k_m is the mechanical stiffness represented by the stiffness of each mechanical structure related to the grinding system:

$$\frac{1}{k_m} = \frac{1}{k_s} + \frac{1}{k_w} + \frac{1}{k_{wo}} + \cdots = \sum_{i=1}^{n} \frac{1}{k_{mi}} \tag{8}$$

where k_{mi} is the i-th stiffness of the mechanical structure relevant to the grinding system and n is the degrees of freedom. Since each component of mechanical stiffness k_m has a linear spring characteristic, k_m remains a constant during the plunge grinding process. On the other hand, the wheel contact stiffness k_c has the non-linear characteristics referred to as "hard-spring." As a result, the equivalent system stiffness k_{eq} behaves as a non-linear spring, which changes in stiffness value depending on the

grinding conditions. As such, it is crucial to take the spring characteristics at the contact area of the grinding wheel into account in the design of the plunge grinding cycle.

The deflection d_e given by Equation (6) is fed back to Equation (1). Thus, the plunge grinding process can be described as a closed-loop system repeating Equations (1)–(6). By using Equations (3)–(5), Equation (6) can be rewritten as follows:

$$d_e(t) = \frac{c \cdot \pi \cdot d_w \cdot b \cdot \eta \cdot u}{v_s \cdot k_{eq}} \cdot f_i(t) = T \cdot f_i(t) \tag{9}$$

where T is the time constant of the grinding system.

$$T = \frac{c \cdot \pi \cdot d_w \cdot b \cdot \eta \cdot u}{v_s \cdot k_{eq}}. \tag{10}$$

The time constant T is one of the most critical parameters in the plunge grinding system.

The Laplace transformation of Equations (1)–(6) leads to the following equations:

$$R_w(s) = I_f(s) - D_e(s) \tag{11}$$

$$F_i(s) = s \cdot R_w(s) \tag{12}$$

$$Q_w'(s) = c \cdot \pi \cdot d_w \cdot F_i(s) \tag{13}$$

$$Q_w(s) = b \cdot Q_w'(s) \tag{14}$$

$$F_n(s) = \frac{\eta \cdot u}{v_s} \cdot Q_w(s) \tag{15}$$

$$D_e(s) = \frac{1}{k_{eq}} \cdot F_n(s) \tag{16}$$

where s is the Laplace operator. Actual infeed $R_w(s)$, actual infeed rate $F_i(s)$, SMMR $Q_w'(s)$, normal grinding force $F_n(s)$, and elastic deflection $D_e(s)$ are Laplace functions.

Figure 3 shows a block diagram of the plunge grinding system representing the transfer functions given by Equations (11)–(16). The plunge grinding system can be expressed by a closed-loop feedback system. The transfer function $G(s)$ of the system is represented by:

$$G(s) = \frac{R_w}{I_f}(s) = \frac{1}{\frac{c \cdot \pi \cdot d_w \cdot b \cdot \eta \cdot u}{v_s \cdot k_{eq}} s + 1} = \frac{1}{Ts + 1}. \tag{17}$$
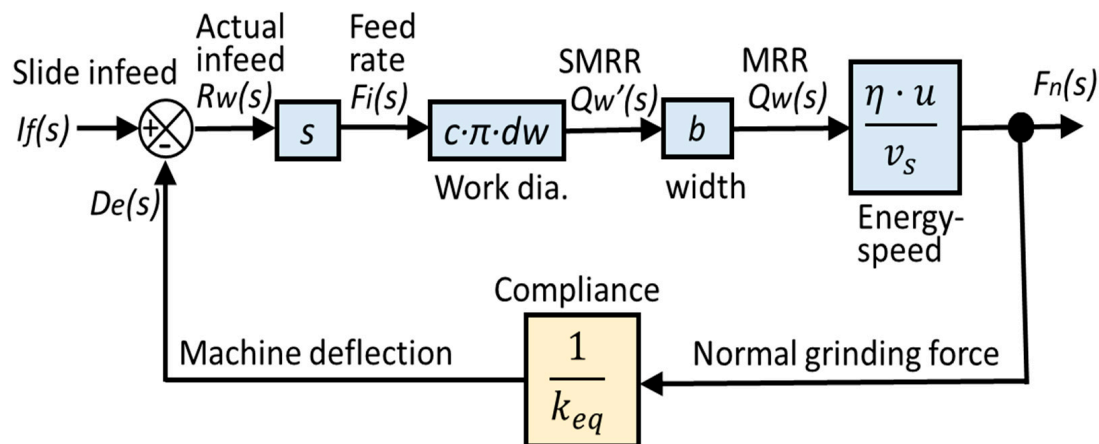

Figure 3. Block diagram of the plunge grinding system.

Thus, plunge grinding can be represented by a first-order lag system with the time constant T given by Equation (10). The cut-off frequency f_c (Hz) of the plunge grinding system is represented by:

$$f_c = \frac{1}{2\pi T}.$$
(18)

2.2. Analysis of Plunge Grinding Cycle

The plunge grinding cycle starts with a rapid forward infeed of the slide from the home position. Typically, the slide feed rate is then changed for rough, semi-finish or finish grinding. After infeed grinding, spark-out grinding is performed in order to reduce the elastic deflection of the grinding system, followed by the rapid retraction of the slide to the home position. To study the effect of the wheel's contact stiffness on the plunge grinding process, this paper focuses on a primary grinding cycle consisting of plunge grinding with a constant infeed rate followed by spark-out grinding.

The diagram in Figure 4a depicts the plunge grinding operation. The infeed slide is rapidly fed forward to position P from the home position H. Then, the infeed rate is changed to a constant infeed rate I_p at point P. At some point O, which is determined by the size of the incoming workpiece, the grinding wheel mounted on the slide contacts the workpiece at the infeed rate I_p and plunge grinding starts. At position A, the slide infeed is stopped and spark-out grinding starts. At point B, the slide is rapidly retracted to the home position H. Figure 4b shows the primary cycle with plunge grinding time t_p and spark-out time $(t_s - t_p)$.
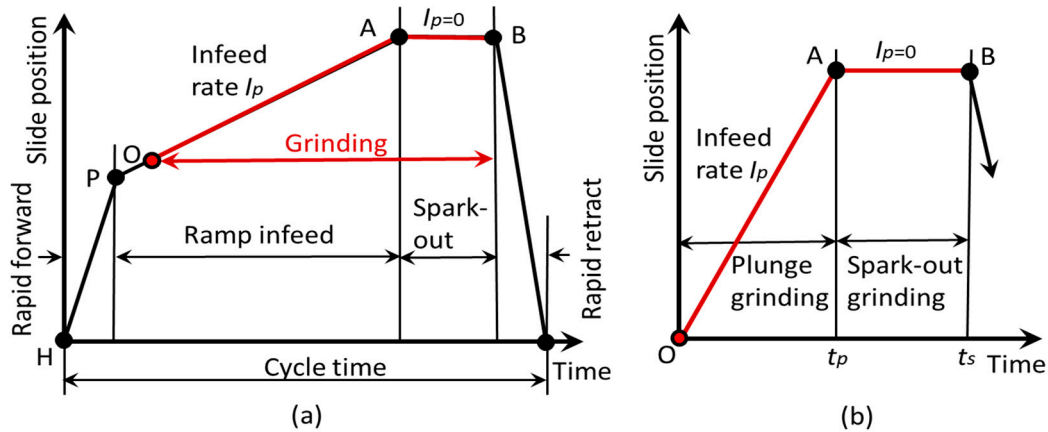

Figure 4. Plunge grinding cycle. (**a**) Diagram of plunge grinding operations; (**b**) Primary cycle of plunge grinding.

During plunge grinding $(0 \le t \le t_p)$, the actual feed rate $f_i(t)$ can be obtained by the following equations [27]:

$$0 \le t \le t_p : \ f_i(t) = I_p\left(1 - e^{-\frac{t}{T}}\right).$$
(19)

$$t_p \le t \le t_s : \ f_i(t) = I_p\left(1 - e^{-\frac{t_p}{T}}\right) \cdot e^{-\frac{(t-t_p)}{T}}.$$
(20)

The actual infeed position $r_w(t)$ is:

$$0 \le t \le t_p : \ r_w(t) = I_p\left[t - T\left(1 - e^{-\frac{t}{T}}\right)\right].$$
(21)

$$t_p \le t \le t_s : \ r_w(t) = I_p\left[t_p - T\left(e^{-\frac{(t-t_p)}{T}} - e^{-\frac{t_p}{T}}\right)\right].$$
(22)

The normal grinding force $F_n(t)$ is:

$$0 \le t \le t_p : \ F_n(t) = I_p \cdot k_{eq} \cdot T\left(1 - e^{-\frac{t}{T}}\right).$$
(23)

$$t_p \le t \le t_s : \ F_n(t) = I_p \cdot k_{eq} \cdot T \left(1 - e^{-\frac{t_p}{T}} \right) \cdot e^{-\frac{(t-t_p)}{T}}. \tag{24}$$

The grinding power $P_g(t)$ is:

$$0 \le t \le t_p : \ P_g(t) = \frac{v_s}{\eta} \cdot I_p \cdot k_{eq} \cdot T \left(1 - e^{-\frac{t}{T}} \right). \tag{25}$$

$$t_p \le t \le t_s : \ P_g(t) = \frac{v_s}{\eta} \cdot I_p \cdot k_{eq} \cdot T \left(1 - e^{-\frac{t_p}{T}} \right) \cdot e^{-\frac{(t-t_p)}{T}}. \tag{26}$$

The deflection $d_e(t)$ causing the size and roundness error is obtained by:

$$0 \le t \le t_p : \ d_e(t) = I_p \cdot T \left(1 - e^{-\frac{t}{T}} \right). \tag{27}$$

$$t_p \le t \le t_s : \ d_e(t) = I_p \cdot T \left(1 - e^{-\frac{t_p}{T}} \right) \cdot e^{-\frac{(t-t_p)}{T}}. \tag{28}$$

When plunge grinding time t_p is long enough compared to time constant T, the above Equations (20), (22), (24), and (26) for spark-out grinding can be approximately represented by the following equations:

$$t_p \le t \le t_s : \ f_i(t) \cong I_p \cdot e^{-\frac{(t-t_p)}{T}}. \tag{29}$$

$$t_p \le t \le t_s : \ r_w(t) \cong I_p \left(t_p - T \cdot e^{-\frac{(t-t_p)}{T}} \right). \tag{30}$$

$$t_p \le t \le t_s : \ F_n(t) \cong I_p \cdot k_{eq} \cdot T \cdot e^{-\frac{(t-t_p)}{T}}. \tag{31}$$

$$t_p \le t \le t_s : \ P_g(t) \cong \frac{v_s}{\eta} \cdot I_p \cdot k_{eq} \cdot T \cdot e^{-\frac{(t-t_p)}{T}}. \tag{32}$$

$$t_p \le t \le t_s : \ d_e(t) \cong I_p \cdot T \cdot e^{-\frac{(t-t_p)}{T}}. \tag{33}$$

Figure 5 is an example simulation of the plunge grinding process. The actual slide position $r_w(t)$ (Figure 5a) is calculated by Equations (21) and (22). The actual slide position delays the command and gradually catches up. Eventually, it attains the same slope as the command feed. The asymptote of the actual infeed curve intersects at time T on the horizontal axis. The position difference between the command feed and the actual feed represents the system deflection and is also the size error. The deflection is reduced with increased spark-out time. The grinding power $P_g(t)$ found by Equations (25) and (26) is the response to the ramp infeed command with a constant rate and the no-infeed command for the spark-out.
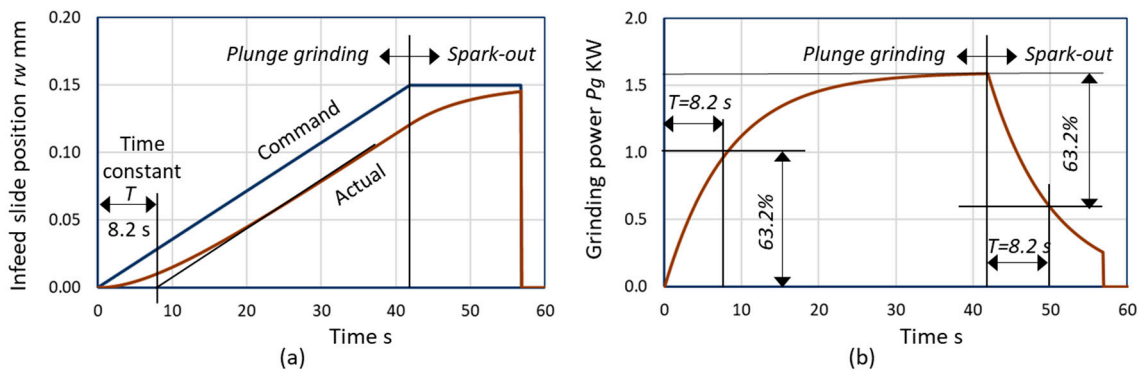

Figure 5. Simulation of plunge grinding processes (conditions: $c = 1.0$, $dw = 177.8$ mm, $b = 30$ mm, vs. $= 45$ m/s, $\eta = 2.0$, $keq = 2421$ N/mm, $u = 26.7$ J/mm^3, $S = 0.3$ mm, $Qw' = 2.0$ mm^3/mm·s, $Ip = 3.58$ μm/s, $tp = 41.9$ s, $ts = 56.9$ s). (**a**) Infeed slide position; (**b**) Grinding power.

The power is gradually increased and finally reaches a constant value. The time constant T is defined as the time when the power reaches 63.2% ($1 - e^{-1} = 0.632$) of the final value. The definition of T can be applied to the spark-out grinding shown in Figure 5b. The transient curves of other parameters, including the actual infeed rate $f_i(t)$, the normal grinding force $F_n(t)$, and the deflection $d_e(t)$, follow the curve of Figure 5b.

2.3. The Effect of Grinding Wheel Contact Stiffness on the Plunge Grinding Process

As mentioned above, system stiffness k_{eq} consists of a constant mechanical stiffness k_m and contact stiffness k_c of the grinding wheel with non-linear characteristics. In this section, the effect of system stiffness (particularly wheel contact stiffness k_c) on the plunge grinding process is discussed.

Figure 6 shows the effect of system stiffness on the plunge grinding process. The response of the grinding power P_g is increased with increased system stiffness. Accordingly, the greater the system stiffness k_{eq}, the shorter the time constant T. In the design of a plunge grinding cycle, the spark-out time can be reduced by increasing system stiffness.
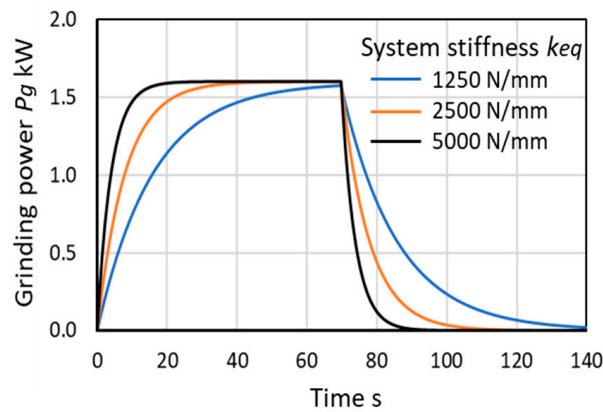

Figure 6. The effect of system stiffness on the plunge grinding process.

Figure 7 presents the effect of system stiffness k_{eq} on the time constant T. T becomes longer where k_{eq} becomes smaller. By using Equations (7) and (10), the time constant T can be rewritten as follows:

$$T = F\left(\frac{1}{k_m} + \frac{1}{k_c}\right) = T_m + T_c. \tag{34}$$

$$F = \frac{F_n}{f_i} \tag{35}$$

where F is the ratio of normal grinding force F_n to infeed rate f_i.
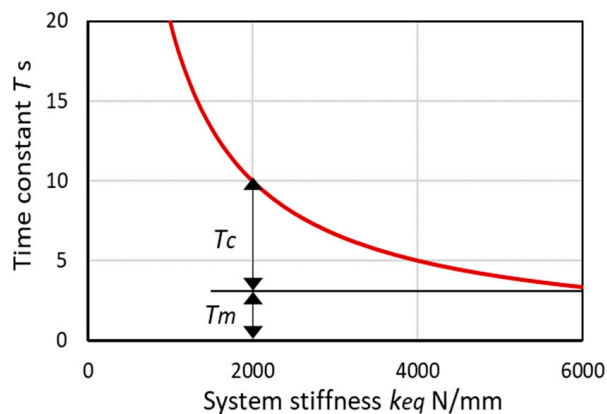

Figure 7. The effect of system stiffness on the time constant.

Given that machine stiffness k_m is a constant, the machine time constant T_m also becomes a constant determined by the grinding machine. On the other hand, wheel contact stiffness k_c has a non-linear characteristic and is dependent on the applied load. In a grinder with a constant machine stiffness k_m, the time constant T is composed of machine time constant T_m and contact time constant T_c, as shown in Figure 7.

3. Measurement of Contact Stiffness of Grinding Wheel

3.1. Experimental Setup

In order to measure the contact stiffness, various grinding wheels were mounted on a center-type cylindrical grinder. A workpiece was supported by the centers of the main work head and tailstock head. The machine and workpiece specifications are shown in Table 1. The specifications of four kinds of grinding wheels are shown in Table 2.

Table 1. Specifications of applied grinding machine and workpiece.

Grinding machine	Center type cylindrical grinder: Tsugami T-PG350 Special feature: Main shaft and tailstock shaft are supported by hydrostatic bearings
Center distance	350 mm
Work swing	280 mm
Grinding wheel	Diameter 405 mm Width 50 mm
Grinding wheel motor	11 kW
Machine net weight	29 kN
Workpiece	Chrome molybdenum steel SCM435, non-hardened Shape: Ground portion diameter 100 mm Width 20 mm Both side shafts: Diameter 20 mm; length 87.5 mm Radial stiffness with center supports at the middle: 10.4 kN/mm

Table 2. Specifications of grinding wheels tested.

Abrasive Material		Abrasive Type	Grain Size #	Grade	Structure	Bond Type
White alundum	Al_2O_3	WA	60	J	8	V: Vitrified
White alundum	Al_2O_3	WA	60	L	8	V: Vitrified
White alundum	Al_2O_3	WA	60	M	8	V: Vitrified
White alundum	Al_2O_3	WA	60	L	8	B: Resinoid

The experimental setup is illustrated in Figure 8. The main shaft and the tailstock shaft were supported by hydrostatic bearings. Pressure gauges were installed to measure the pocket pressures of the hydrostatic bearings. So, the normal load L acting on the contact area between the workpiece and the wheel can be measured by detecting the pressure differences of the pockets in the hydrostatic bearings. Also, a load compensator [28] was attached to the machine. The compensator provided the same force as the detected load L to the workpiece. Therefore, the effective radial stiffness of the workpiece was significantly increased from 10.4 kN/mm to 200 kN/mm by the load compensator. The contact deflection δ_c of the grinding wheel can be found by measuring the deflection δ_s at the flange of the grinding wheel and the workpiece deflection δ_w. The deflections δ_s and δ_w are measured with cantilever type electric micrometers. The estimated measurement error is ±0.2 μm which is accurate enough compared with the amounts of deflections δ_s and δ_w. The micrometers are mounted on the base of the grinding machine. The difference $(\delta_s - \delta_w)$ corresponds to the wheel deflection δ_c.
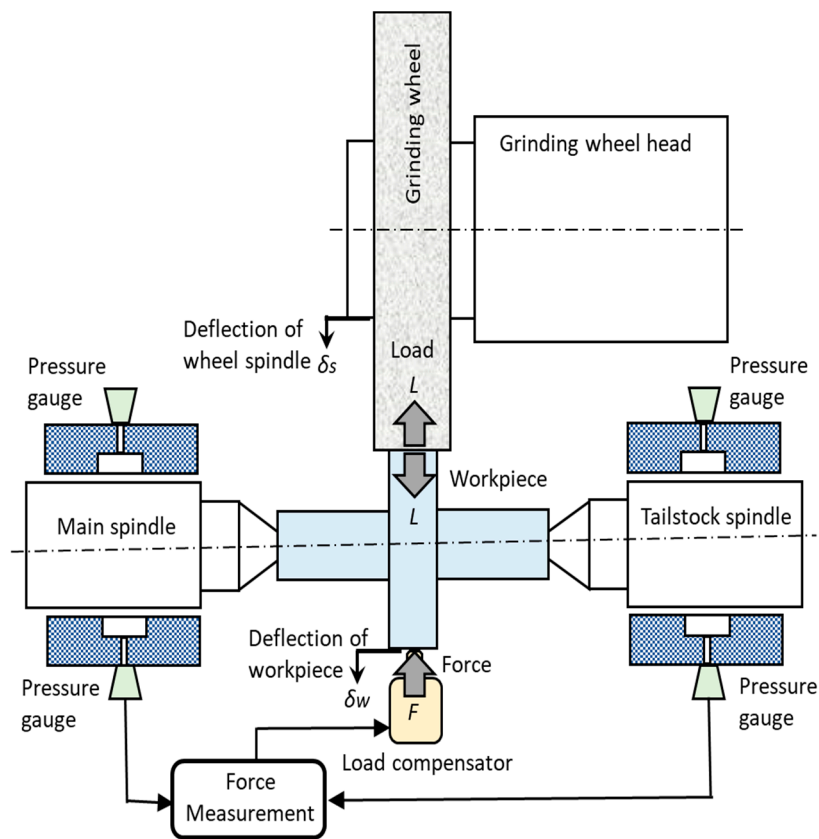
Figure 8. Experimental setup.

3.2. Footprint Method

The workpieces painted black were pressed with a normal load L to the grinding wheel as shown in Figure 8. Both shafts of the workpiece and the wheel were locked in rotation. The contact footprints of the wheel were left on the surface of the workpiece, and the contact length l_c was measured with a microscope. This paper names the method "footprint method".

Figure 9a,b describe the contact length and the contact deflection δ_c for external grinding and internal grinding, respectively. Contact deflection δ_c is approximately expressed by:

$$\delta_c \cong \frac{l_c{}^2}{4 \cdot d_{eq}}. \tag{36}$$

where d_{eq} is the equivalent wheel diameter represented by:

$$d_{eq} = \frac{d_w d_s}{d_w \pm d_s} \tag{37}$$

where d_s and d_w are the diameters of grinding wheel and workpiece, respectively. The + sign is used for external grinding and the − sign for internal grinding.

In the external grinding shown in Figure 9a, d_{eq} is always less than both d_s and d_w. In the internal grinding shown in Figure 9b, d_{eq} is always bigger than d_s and d_w. Typically, the contact length l_c for internal grinding is much longer than that of external grinding. The contact situation can be considered equivalent to one in which a flat-plate workpiece is ground by a surface grinder with the grinding wheel (diameter d_{eq}), as shown in Figure 9c.

Figure 10 shows microscopic images of the footprints when the grinding wheel (WA60J8V) was pressed to the workpiece with a varying specific load L'. Increasing load L' increases not only the band width corresponding to contact length l_c, but also the number of contact marks corresponding to the

number of abrasive grains. As the contact boundary was unclear sometimes, the measurement of the contact length by the microscope does not have high accuracy. The estimated error is ±0.1 mm. The measurement results of the contact length are discussed in the next section.
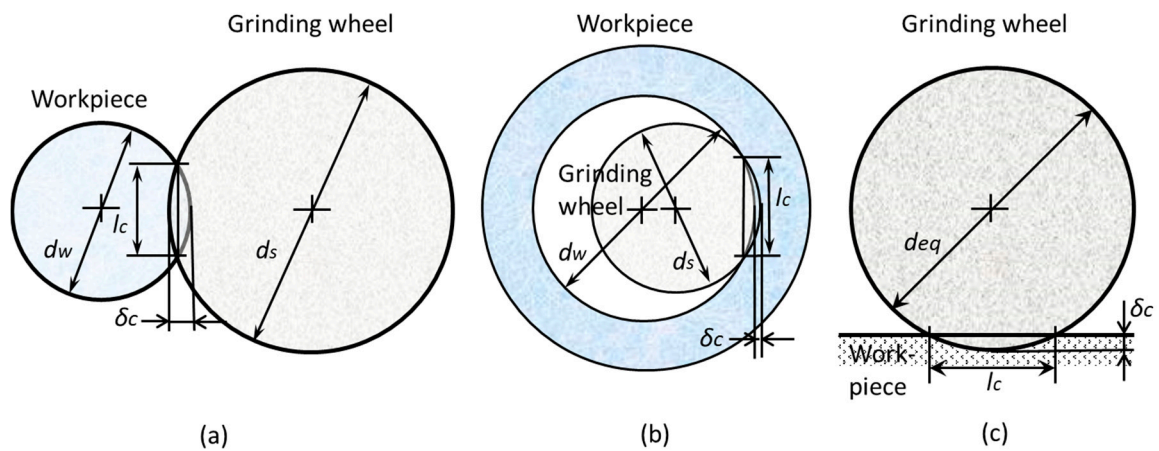

Figure 9. Contact length and deflection. (**a**) External grinding; (**b**) Internal grinding; (**c**) Equivalent wheel diameter.
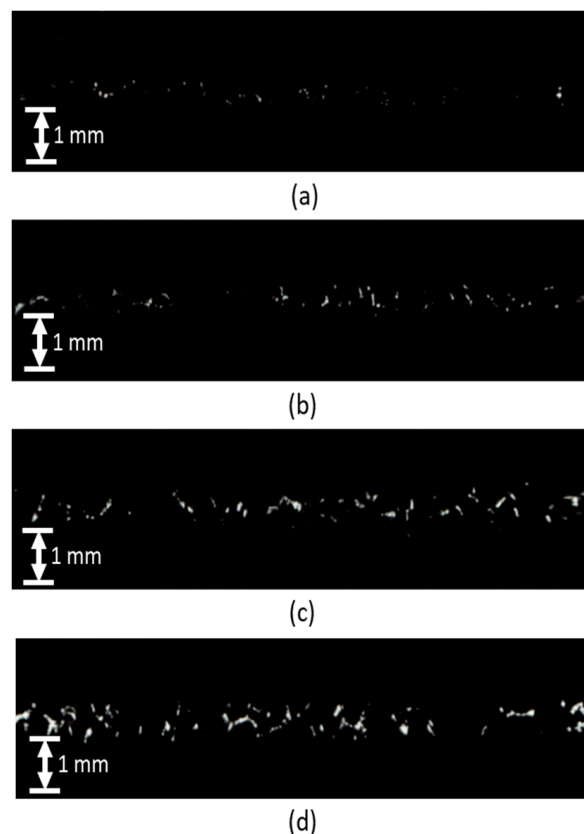

Figure 10. Contact footprint of grinding wheel WA60J8V, $d_s = 195$ mm, $d_w = 98$ mm, $b = 20$ mm. (**a**) 1 N/mm; (**b**) 2.5 N/mm; (**c**) 5 N/mm; (**d**) 10 N/mm.

3.3. Deflection Method

The deflections of δ_s and δ_w were directly measured under loading and unloading conditions. This paper names this method "deflection method". Figure 11a shows the measurement results without the load compensator. When the specific load L' was increased from zero to 22 N/mm, deflection δ_s

increased from zero to point B via point A. At point B, L' gradually reduced to zero via C. During measurement, the deflection δ_w changes O-A'-B'-C'-O. There are small differences in the deflection values between loading and unloading.
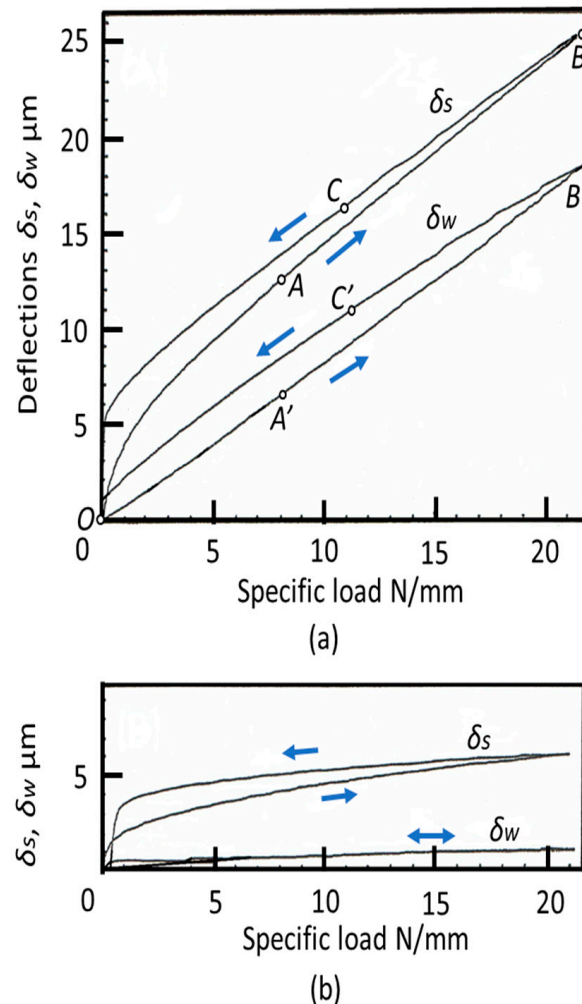

Figure 11. Deflections of wheel and workpiece under loading and unloading with grinding wheel WA60J8V. (**a**) Without load compensator; (**b**) With load compensator.

Figure 11b is the result of the deflection measurements after implementing the load compensator. The deflection δ_w of the workpiece was drastically reduced by the compensator, which also created an improvement in measuring accuracy. In both cases (Figure 11a,b), the hard-spring characteristics were clearly observed in the changes to δ_s, especially at the lower load L', while δ_w linearly changed with load L'. The contact deflection δ_c at load L' is found by $(\delta_s - \delta_w)$ under loading or unloading conditions. It was also observed that the grinding wheel elastically deflected with the load; it behaved like a hard spring at the lower load and like a linear spring at the higher load.

Figure 12a shows the repeatability of the measurement of δ_s. The specific load L' was increased from O to B via A, then L' was reduced to O via C. Then, L' was increased from O to B via D again and was reduced to O via E. The tests were repeated four times. Although there was a difference in δ_s between the first loading and unloading, there was no difference after the second loading. The deflection patterns with the load were repeated and the good repeatability was confirmed. Figure 12b shows the difference in δ_s between the first loading and unloading at the different maximum loads R1, R2, R3, and R4. The difference was seen only at the first loading. After the second loading, there was no difference, as shown in Figure 11b.
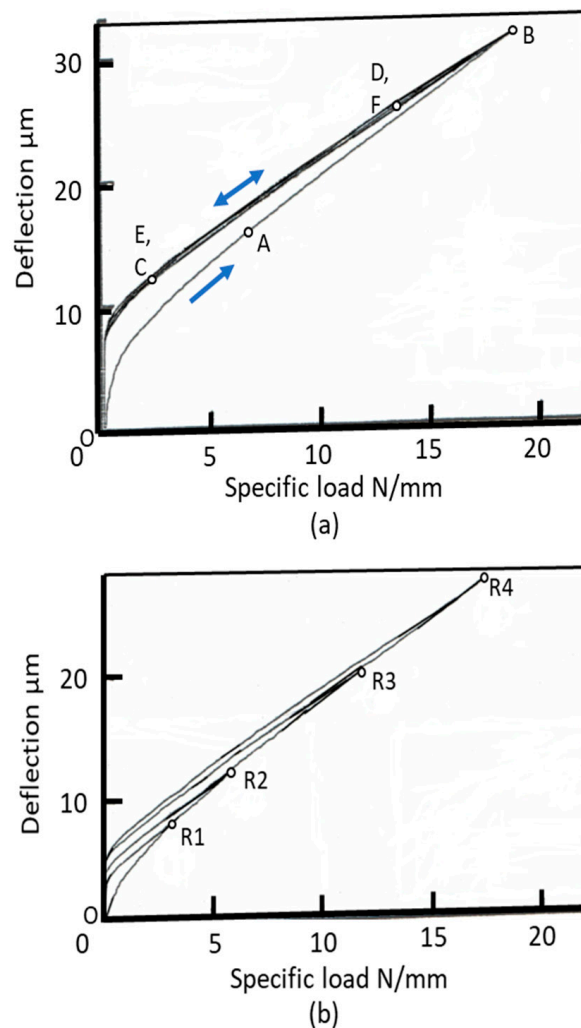
Figure 12. Repeatability of the measurements of wheel deflection, grinding wheel WA60J8V. (**a**) Same load cycle; (**b**) Incremental load cycle.

3.4. Modeling of Grinding Wheel Contact Deflection

Figure 13 compares the measurement results of wheel contact deflection δ_c obtained by the deflection method with the load compensator and the footprint method. The deflections δ_c found by the deflection method are greater than the footprint values at each specific load L'. Although the deflection method has much higher measurement accuracy than the footprint method, the difference is obvious. It can be considered that the footprint method's results reflect only the deflection of the local contact area, while the deflection method's results contain the deflections of both the local contact area and the wheel body from the contact point to the bore with wheel flange. Both methods reveal that wheel deflection is composed of non-linear characteristics at the lower range of the load and linear spring characteristics at the higher range of the load. In this case, the critical specific load is about 3 N/mm.

From the experimental observations, it is assumed that the contact stiffness of the grinding wheel is composed of a non-linear spring and a liner spring. Figure 14a illustrates the wheel-workpiece inference with the equivalent wheel diameter d_{eq}. The contact deflection δ_c under the normal load L is represented by a hard spring shown in Figure 14b. It is assumed that the hard spring can be replaced with the series connection of two springs shown in Figure 14c. One has the non-linear spring constant k_a, which represents the local stiffness of the contact area. The other has the linear spring constant k_b, which represents the body stiffness of the grinding wheel itself.
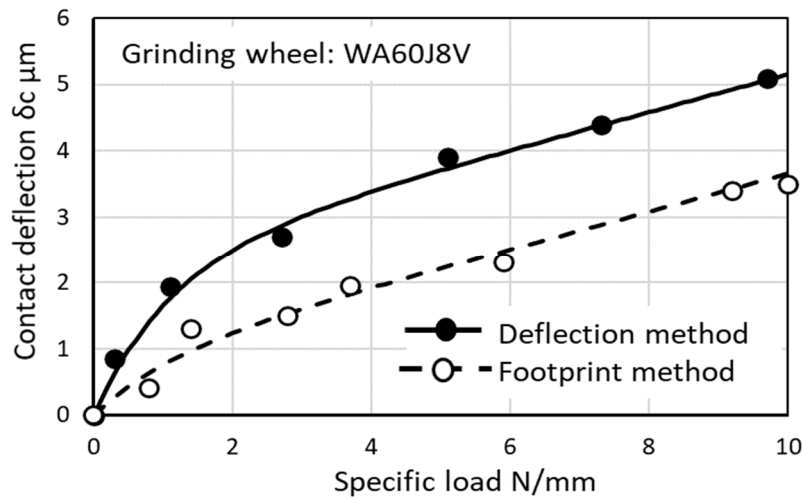
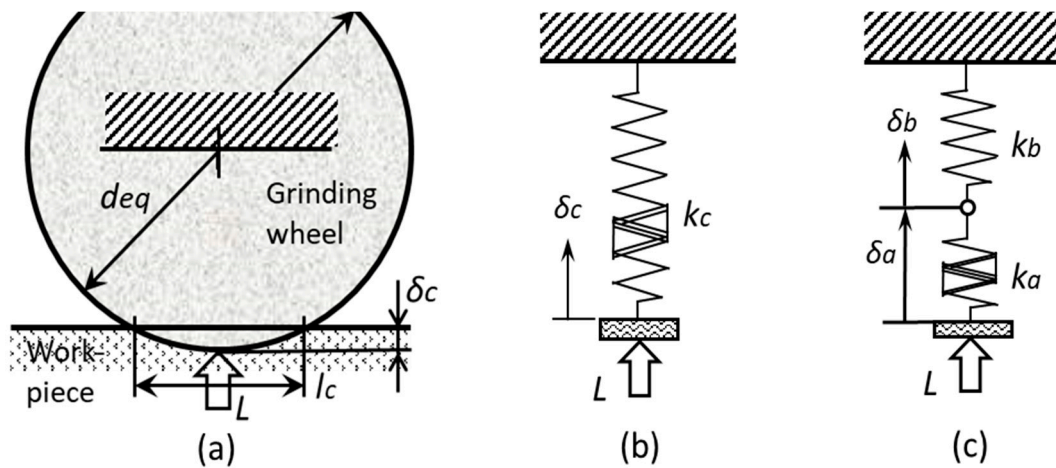**Figure 13.** Comparison of wheel deflections obtained by the deflection method and the footprint method.

Figure 14. Modeling of the contact stiffness of the grinding wheel. (**a**) Contact of wheel with workpiece; (**b**) Model of contact stiffness; (**c**) Series connection of linear and non-linear springs.

In Figure 14c, contact deflection δ_c is expressed by:

$$\delta_c = \delta_a + \delta_b \tag{38}$$

where δ_a is the deflection of the non-linear spring with k_a, and δ_b is the deflection of the linear spring with k_b. As δ_a represents the non-linear deflection with load L, it is assumed that deflection δ_a can be represented by:

$$\delta_a = A\left(1 - e^{-\frac{L'}{S}}\right) \tag{39}$$

where A and S are constants and L' is the specific load per unit contact width. It is also assumed that the body of the grinding wheel has a spring constant of k_b. So, deflection δ_b is expressed by:

$$\delta_b = \frac{L'}{k_b'} \tag{40}$$

where k_b' is the specific spring stiffness per unit width. Therefore, contact deflection δ_c can be rewritten as follows:

$$\delta_c = A\left(1 - e^{-\frac{L'}{S}}\right) + \frac{L'}{k_b'}. \tag{41}$$

Differentiating both sides of Equation (41) provides the specific compliance $d\delta_c/dL'$ of the grinding wheel.

$$\frac{d\delta_c}{dL'} = \frac{A}{S}e^{-\frac{L'}{S}} + \frac{1}{k_b'}. \tag{42}$$

Therefore, specific contact stiffness k_c' per unit width can be expressed by:

$$k_c' = 1/\left[\frac{A}{S}e^{-\frac{L'}{S}} + \frac{1}{k_b'}\right]. \tag{43}$$

Also, the non-linear contact stiffness of local area per unit width k_a' is:

$$k_a' = \frac{S}{A}e^{\frac{L'}{S}}. \tag{44}$$

In Figure 13, the best fit curves for both methods were found by using Equation (41). The solid line is for the deflection method and the dotted line is for the footprint method. The parameters shown in Table 3 were used for the calculations of δ_c. k_b' represents the wheel body stiffness and parameter A shows the degree of local deflection δ_a. Parameter S expresses the degree of raising curve at the lower specific load L'.

Table 3. Parameters for representing the contact deflection of the grinding wheel WA60J8V.

Parameter	Unit	Deflection Method	Footprint Method
k_b'	kN/mm·mm	3.5	3.5
A	μm	2.3	0.8
S	N/mm	1.1	1.1

The specific contact stiffnesses for both methods were calculated by using Equation (43), as shown in Figure 15. At $L' > 6$ N/mm·mm, both methods provide the same contact stiffness. At $L' < 6$ N/mm·mm, the deflection method provides lower contact stiffness than the footprint method. The specific contact stiffness k_c' was 3.5 kN/mm·mm at $L' > 6$ kN/mm. At $L' = 2$ kN/mm, 1.5 kN/mm·mm and 2.5 kN/mm·mm were obtained by the deflection method and the footprint method, respectively.
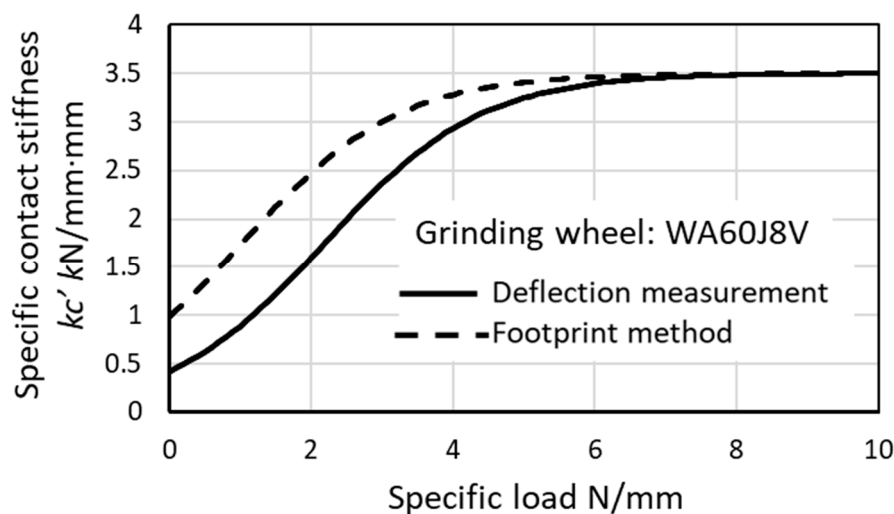

Figure 15. Specific contact stiffness of grinding wheel.

Based on the contact stiffness model, the specific contact stiffness k_c' is composed of two components, k_a' for local deflection and k_b' for wheel body deflection. Figure 16 shows the specific

contact stiffness k_c' obtained by the deflection method, where k_a' was found by Equation (44) and k_b' was set to 3.5 kN/mm·mm. The specific local area stiffness k_a' shows heavy hard-spring characteristics such as lower stiffness at $L' < 2$ kN/mm and higher stiffness at $L' > 3$ kN/mm. The dominant component of k_c' is k_a' at the lower load $L' < 2$ kN/mm and k_b' at the higher load $L' > 4$ kN/mm.
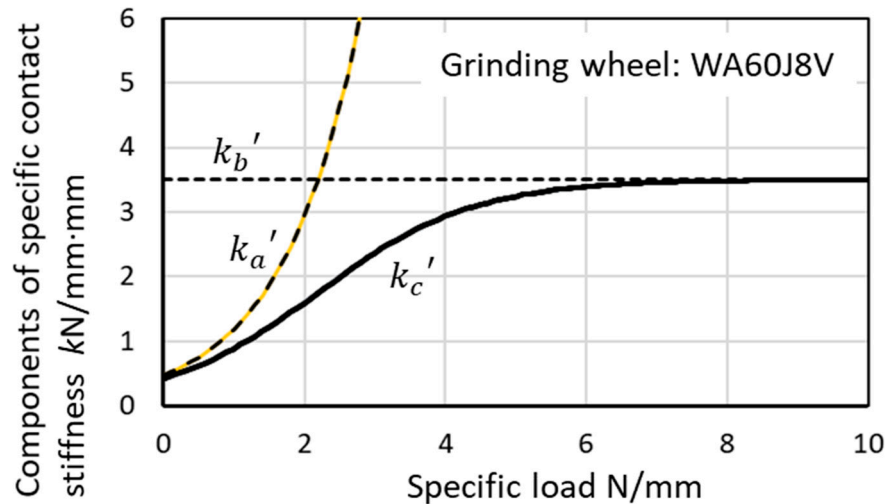

Figure 16. Components of specific contact stiffness.

3.5. Measurement Results of Grinding Wheel Contact Stiffness

The contact deflections δ_c of four kinds of grinding wheels shown in Table 2 were measured by the deflection method with the load compensator. Figure 17 shows the measurement results. The best fit curves were found by using the parameters shown in Table 4. As seen in Figure 17, all grinding wheels exhibited heavy hard-spring behavior at the lower load and a liner spring nature at the higher load. The resinoid bond wheel WA60L8B exhibited the greatest deflection among the tested wheels and the vitrified bond wheel WA60L8V gave the smallest. In wheels WA60M8V and WA60L8B, the reduction of the deflection appeared at L'> 8 kN/mm. It seems that a structural change in the grinding wheels occurred at the higher load. These phenomena should be investigated in the future.
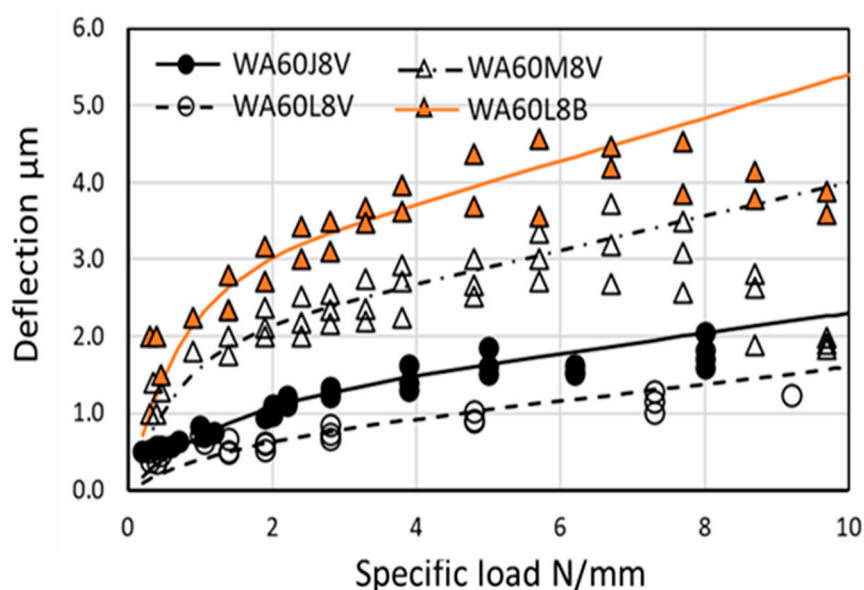

Figure 17. Contact deflection of various Al_2O_3#60 grinding wheels.

Table 4. Parameters of various grinding wheels obtained by the deflection measurements.

Parameter	Unit	WA60J8V	WA60L8V	WA60M8V	WA60L8B
k_b'	kN/mm·mm	7.7	9.1	4.5	3.6
A	Mm	1	0.5	1.8	2.6
S	N/mm	1.2	1.2	0.7	0.7

The contact stiffnesses were found by Equation (43) from the deflection curves shown in Figure 17. Figure 18 shows the specific contact stiffness k_c' of various Al_2O_3#60 grinding wheels. The WA60L8V wheel had the highest contact stiffness, followed by the WA60J8V and WA60M8V wheels. The resinoid bond WA60J8B wheel had the lowest stiffness among them. At the specific load $L' < 2$ kN/mm, all grinding wheels exhibited very low contact stiffness at the range of $0 < L' < 4$ N/mm. At the higher load $L' > 4$ N/mm, the contact stiffness reached a constant level.
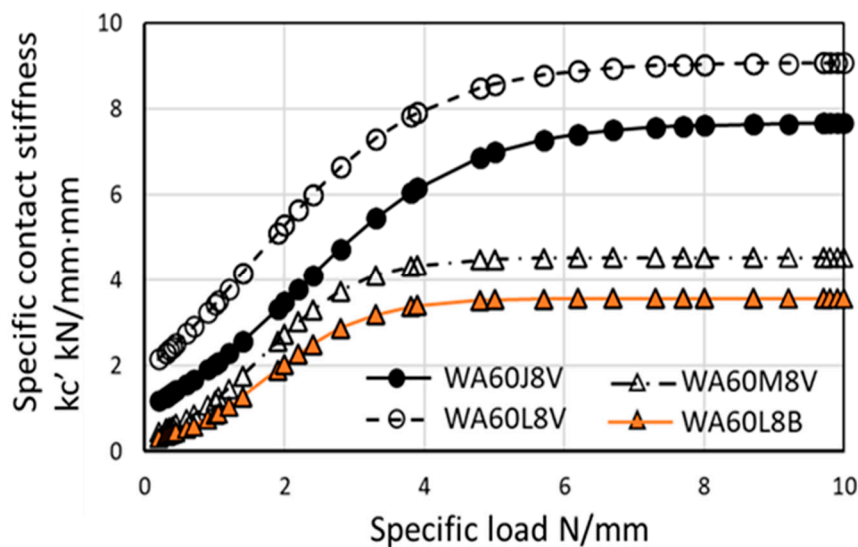

Figure 18. Contact stiffness of various Al_2O_3 #60 grinding wheels.

Figure 19 shows the influence of accumulative SMR (specific material removal) on the deflection of the WA60M8V wheel. The dressing conditions are single point dresser, dressing lead 0.1 mm/rev., and adress depth of cut 20 μm. The best fit curves are drawn in the figure. The deflection after dressing was reduced and the deflection curve changed with increased SMR. No clear trend was observed. After dressing, the deflection curves gradually changed up and down according to the accumulative SMR progression. The G-ratio (grinding ratio) for monitoring the wear progress was not investigated in this study.

Figure 20 shows the changes in contact stiffness after dressing. The contact stiffness was found by applying the parameters shown in Table 5 to Equation (43). The contact stiffness at the lower range of load ($L' < 1.5$ kN/mm) was very low and no corresponding change occurred. But, at the higher range ($L' > 4$ kN/mm), the contact stiffness increased significantly by 20–50% after dressing.

Table 5. Parameters of wheel deflection taken during specific material removal (SMR) progression.

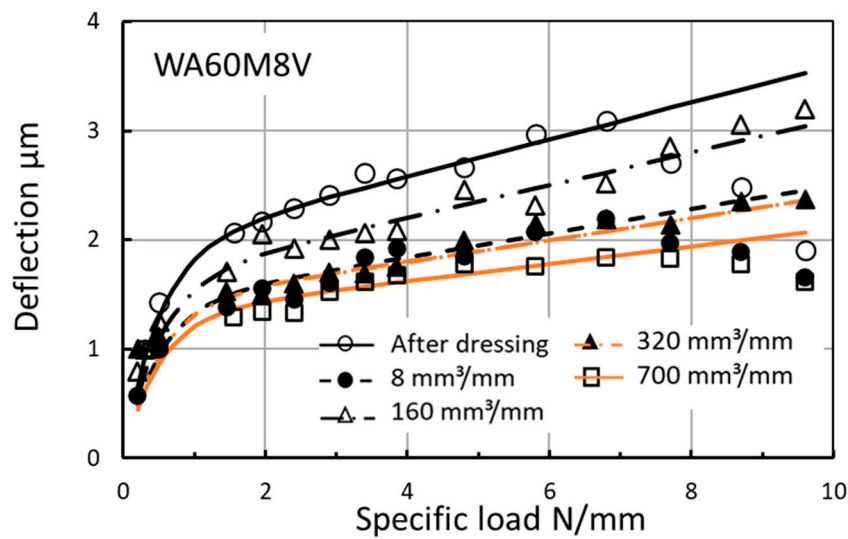| Item	Unit	Obtained Parameter				
SMR	mm³/mm	0	8	160	320	700
k_b'	kN/mm·mm	5.9	9.1	6.7	10	12.5
A	μm	1.9	1.4	1.6	1.4	1.3
S	N/mm	0.5	0.5	0.5	0.5	0.5

Figure 19. The effect of accumulative specific material removal on contact deflection.
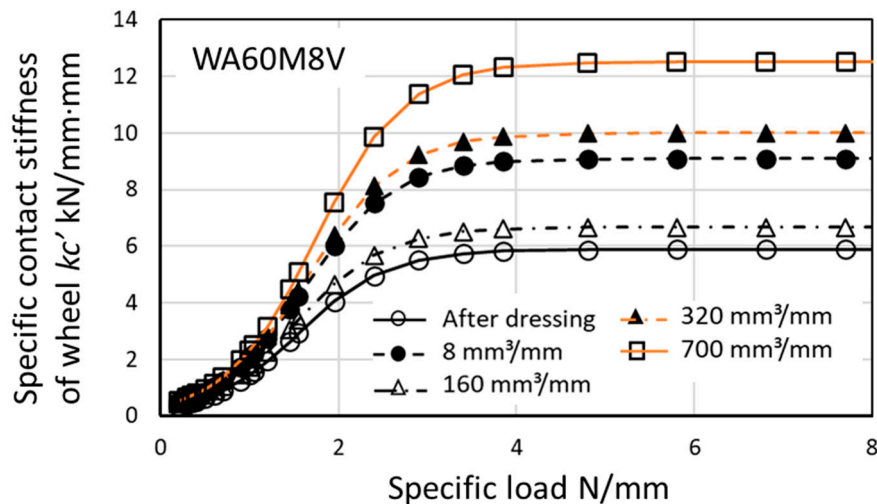

Figure 20. The effect of accumulative specific material removal on contact stiffness.

4. Results of Plunge Cylindrical and Centerless Grinding Tests

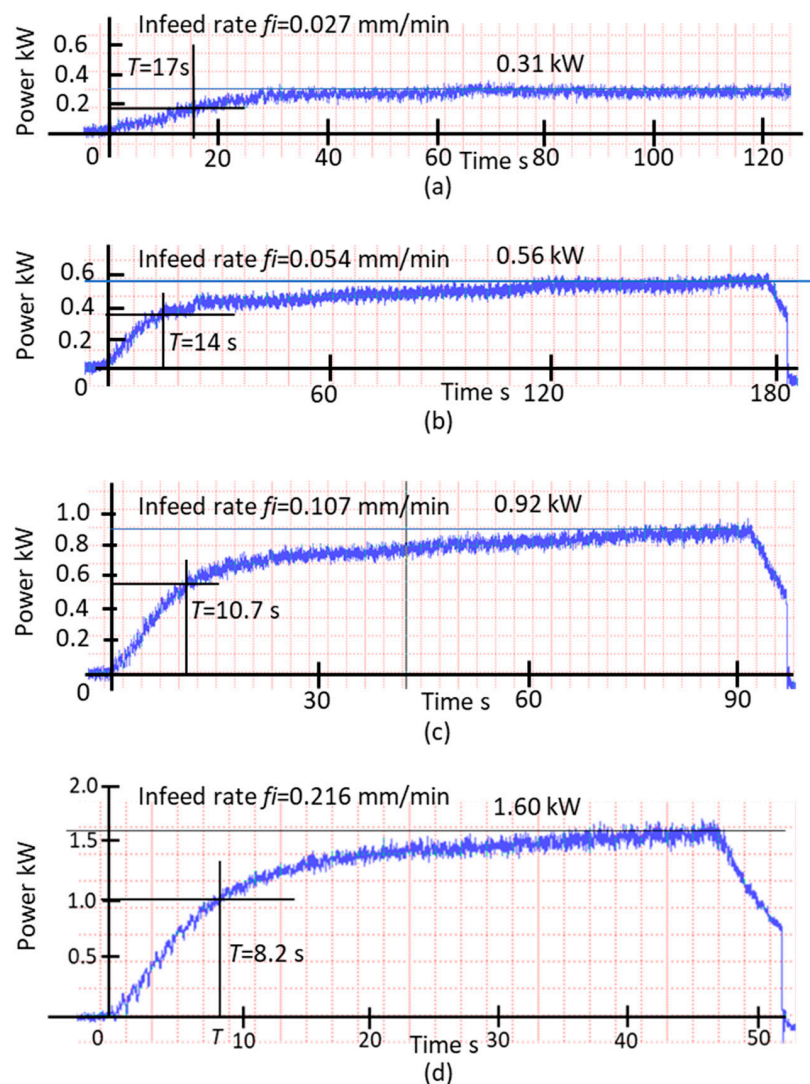### 4.1. Test Results of Plunge Cylindrical Grinding

Given that the contact stiffness k_c of the grinding wheel largely relies on the specific normal load L', it is expected that the normal grinding force F_n affects the time constant T in the plunge grinding system because T is a function of k_c (see Equation (34)). Plunge cylindrical grinding (c = 1.0) tests were carried out with various infeed rates f_i, and grinding power P_g was measured during the grinding process. The grinding conditions are shown in Table 6.

Figure 21 shows the ramping up of the grinding power from start to steady state during the plunge grinding process. At SMRR Q_w' = 0.25 mm³/mm·s, which was very low (Figure 21a), the grinding power slowly built up and finally reached a steady state power of 0.31 kW. From the power curve, the time constant T of 17 s was measured. The time constant became shorter with increased SMRR Q_w'. At Q_w' = 2.0 mm³/mm·s, the time constant T was shortened and T = 8.2 s was obtained.

The reason the time constant gets shorter with increased Q_w' is that contact stiffness k_c becomes greater at the higher normal grinding force F_n. The estimated range of the specific normal grinding force F_n' is 0.46~2.36 N/mm, which can be considered as the lower specific load L'. In the load range, contact stiffness k_c clearly exhibits a hard-spring nature and the contact time constant Tc of Equation (34) significantly changes.

Table 6. Grinding conditions of plunge cylindrical grinding.

Item	Conditions
Grinding machine	Universal cylindrical grinder: Heald 2EF Cinternal
Grinding method	Chuck type cylindrical grinding
Workpiece	Material: Through-hardened 52100 (HRC58) Diameter: 177.8 mm Width: 30 mm
Grinding wheel	Specification: A70KmV Diameter: 127 mm Width: 86.4 mm
Grinding speed, ratio	Grinding speed: 45 m/s, Speed ratio: 1/100

Figure 21. Experimental results of plunge cylindrical grinding and the time constant. (**a**) $Q_w' = 0.25$ mm^3/mm·s; (**b**) $Q_w' = 0.5$ mm^3/mm·s; (**c**) $Q_w' = 1.0$ mm^3/mm·s; (**d**) $Q_w' = 2.0$ mm^3/mm·s.

4.2. Test Results of Plunge Centerless Grinding

Table 7 delineates the grinding conditions for plunge centerless grinding (c = 0.5) of glass workpieces. The regulating wheel spindle of the grinding machine was supported by hydrostatic bearings and the grinding forces were measured by detecting the pocket pressures of the bearings [29].

Table 7. Grinding conditions of plunge centerless grinding.

Item	Conditions
Grinding machine	Centerless grinding machine
Workpiece	Glass HV500 Diameter: 12.4 mm Length: 66 mm
Grinding wheel	Specification: SiC, GC 100 LmV Diameter: 455 mm Width: 150 mm
Regulating wheel	Specification: A150RR Diameter: 255 mm Rotational speed: 12.7 rpm
Grinding conditions	Blade angle: 30° Center height angle: 6.8° Grinding speed: 29 m/s

Figure 22 shows test results of plunge centerless grinding with different infeed rates. The periodic fluctuations observed on the force curves were due to the radial runout of the regulation wheel rotation. Taking the average of the fluctuations, the time constant T was measured for each plunge grinding operation. The time constant was prolonged when the specific material removal rate was reduced.
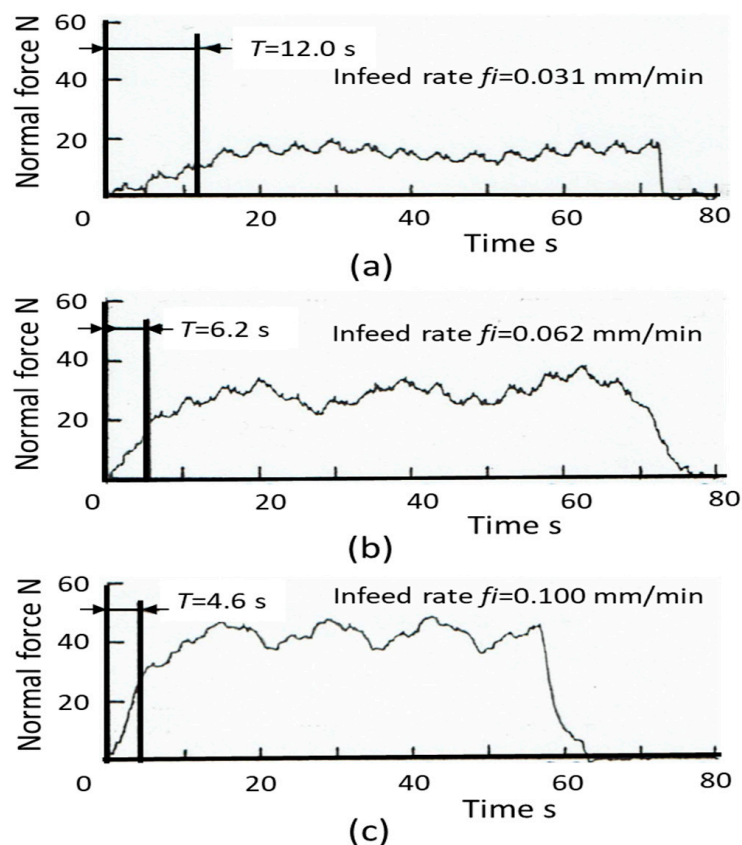

Figure 22. Experimental results of plunge centerless grinding and the time constant. (**a**) $Q_w' = 0.01$ mm^3/mm·s; (**b**) $Q_w' = 0.02$ mm^3/mm·s; (**c**) $Q_w' = 0.0325$ mm^3/mm·s.

The grinding tests were repeated many times with a specific normal load range of $L' = 0.06{\sim}0.7$ N/mm (which is considered a very light load). The results are summarized in Figure 23. The time constant T converges at about 4 s at SMRR $Q_w' > 0.03$ mm^3/mm·s. The converged time (about 4 s) corresponds

to the machine time constant T_m described in Figure 7. By contrast, the time constant was rapidly prolonged where the SMRR was reduced. It reaches 28 s at SMRR $Q_w' = 0.002$ mm^3/mm·s. In this case, the contact time constant T_c becomes 24 s. The increased T_c comes from the reduced contact stiffness created by the reduced contact load. This result clearly reveals that the time constant T is significantly increased with reduced SMRR Q_w'.
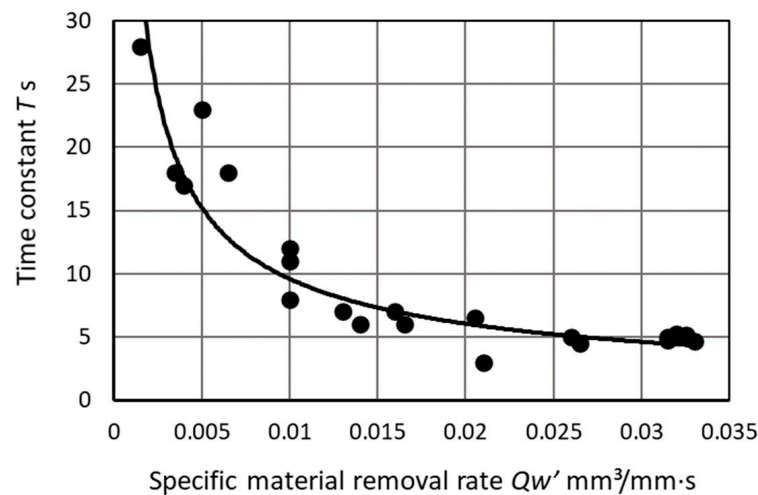

Figure 23. The effect of specific material removal rate on the time constant in plunge centerless grinding.

5. Validation and Discussion

The plunge cylindrical grinding (c = 1.0) test results shown in Figure 21a–d were simulated using Equations (19)–(28) for the primary grinding cycle shown in Figure 4b. The simulation results are shown in Figure 24a–d. Also, Figure 25a–c show the simulations of experimental results obtained by plunge centerless grinding (c = 0.5) shown in Figure 22a–c. In all simulations of plunge grinding operations, the transient behaviors in build-up during ramp infeed and the reduction during spark-out are almost identical to the experimental results, and the levels in steady state and the time constant are excellent matches to the experimental results. These correlations indicate that the proposed model can accurately predict critical parameters such as forces F_t and F_n, power P_g, machine deflection de, equivalent system stiffness keq, and time constant T during both plunge cylindrical grinding and centerless grinding.

Table 8 lists the critical parameters obtained by the simulations in Figure 24a–d. The specific energy u for each plunge grinding operation was found, and it was observed that u increased with increased SMRR Q_w'. These phenomena are well known in grinding [30]. The equivalent chip thickness h_{eq} (defined as the ratio of SMRR Q_w' to grinding speed v_s) is a key parameter that affects energy u and the finished surface quality [31]. The system stiffness k_{eq} obtained by the simulation decreased with the decrease in specific normal grinding force F_n'.

Table 8. Critical parameters obtained by the simulations in Figure 23.

Symbol	F_n'	u	T	k_{eq}	$\hat{k}_m$	k_c'
Unit	N/mm	J/mm^3	s	kN/mm	kN/mm	kN/mm·mm
(a)	0.46	41.4	16	1.92	2.47	0.29
(b)	0.83	37.4	14	1.99	2.47	0.34
(c)	1.36	30.7	10.7	2.13	2.47	0.52
(d)	2.36	26.7	8.2	2.42	2.47	4.0

F_n': specific normal grinding force, u: specific energy, T: time constant, k_{eq}: system stiffness, $\hat{k}_m$: estimated machine stiffness, k_c': specific contact stiffness.

From the system stiffness analysis, the machine stiffness of the applied grinder was estimated to $\hat{k}_m$ = 2.47 kN/mm as a constant value. Then, the specific contact stiffness k_c' of the grinding wheel was calculated. k_c' = 4.0 kN/mm·mm was obtained when the infeed rate was highest (Figure 24d). When the infeed rate was slowest (Figure 24a), the specific contact stiffness was significantly reduced to k_c' = 0.29 kN/mm·mm and hard-spring characteristics were clearly exhibited, as expected.

As the result of the reduced system stiffness k_{eq} due to the reduction of contact stiffness k_c, the time constant T drastically increased by over 200% from 8.2 s to 17 s, as predicted by Equation (10). So, when a grinding cycle is designed, the plunge infeed time and spark-out time should be determined by taking into account the influence of the infeed rate on the time constant T.

It is clear that the time constant T significantly changes by 2–2.6 times, as seen in Figures 24 and 25. The amount of change depends on the contact stiffness of the grinding wheel, which relies on contact load L; that is, normal grinding force F_n in this case. When a plunge grinding cycle with a lower infeed rate fi is set up, a long-time constant will be found due to the lower contact stiffness at the lower grinding force Fn. On the other hand, the effect of contact stiffness on the time constant can be ignored when high stock removal conditions with high SMRR Q_w' and high normal grinding force F_n are set up.
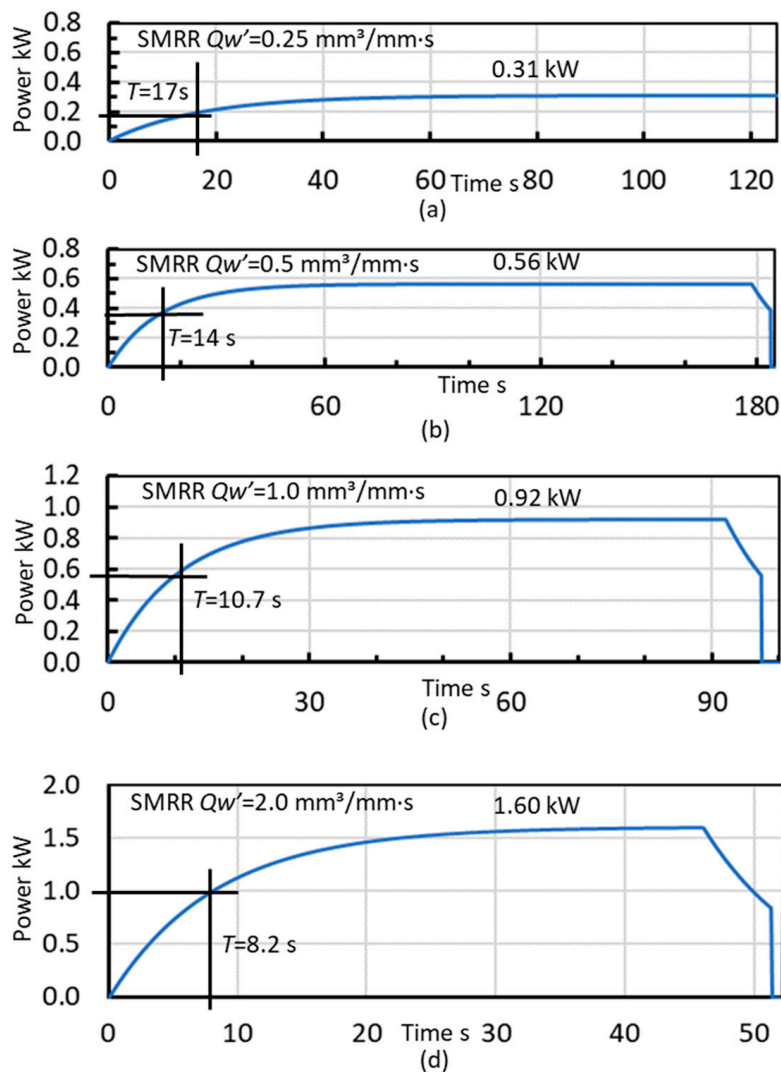

Figure 24. Simulations of plunge cylindrical grinding processes. (**a**) Q_w' = 0.25 mm³/mm·s; (**b**) Q_w' = 0.5 mm³/mm·s; (**c**) Q_w' = 1.0 mm³/mm·s; (**d**) Q_w' = 2.0 mm³/mm·s.
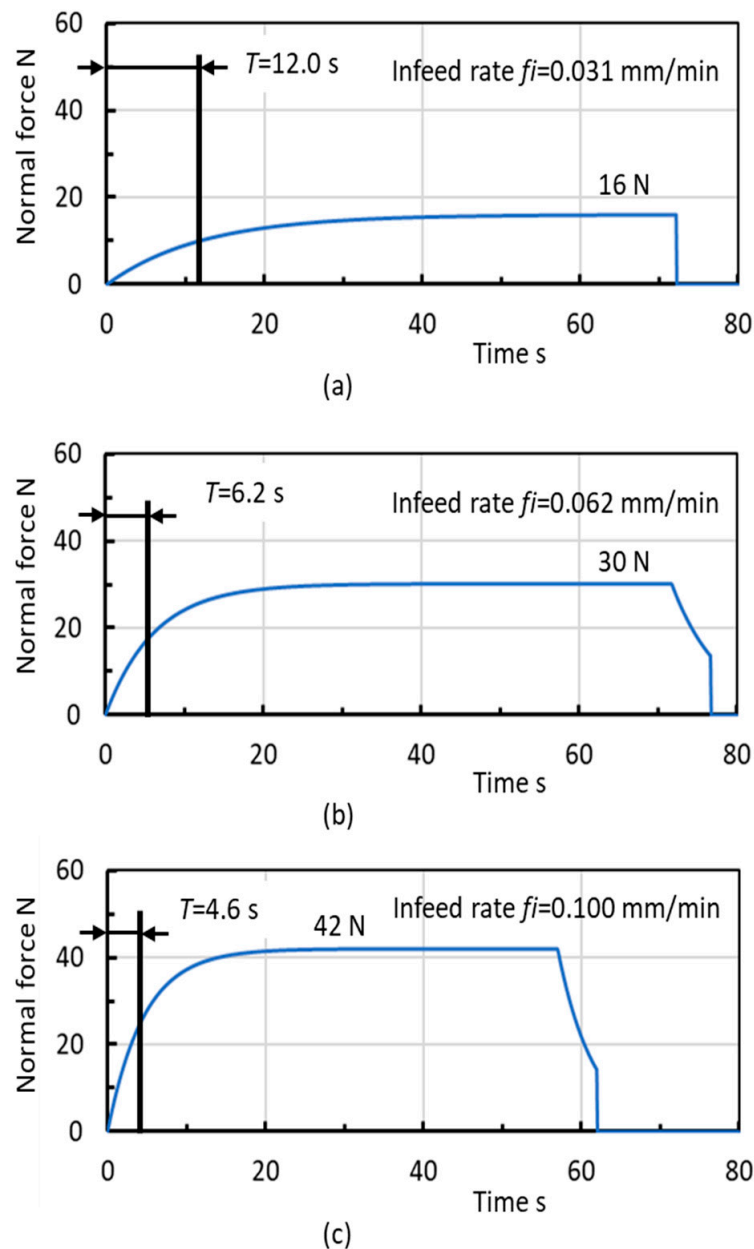
Figure 25. Simulations of plunge centerless grinding. (**a**) $Q_w' = 0.01$ mm³/mm·s; (**b**) $Q_w' = 0.02$ mm³/mm·s; (**c**) $Q_w' = 0.0325$ mm³/mm·s.

In general, the ramp infeed time of the plunge grinding cycle requires at least five times T ($5T$). This setting provides sufficient time for reaching 99.3% of the target level of the steady state $\left(\left(1 - e^{-5}\right) = 0.993\right)$. The spark-out time requires at least three times T ($3T$) in order to reduce the system deflection de by 95% $\left(\left(1 - e^{-3}\right) = 0.950\right)$. Setting the spark-out time to $3T$ affords the grinding operation not only improved size error, but also improved roundness of the finished products. In the plunge grinding operations using Al_2O_3 grinding wheels, the time constant T can be reasonably estimated by using the data of wheel contact stiffness shown in Figures 18 and 20. It allows process engineers to determine the spark-out time and the proper grinding cycle for achieving the required size error and roundness. The design procedures are described in [27].

For high-efficiency and high-precision plunge grinding, it is vital to take the effect of contact stiffness on the plunge grinding process into consideration during the design of the grinding cycle.

6. Conclusions

This paper presented the effect of grinding wheel contact stiffness on the plunge grinding cycle and provided guidelines for the design of the grinding cycle. First, the generalized plunge grinding system (including cylindrical, centerless, shoe-centerless, internal, and shoe-internal grinding) was explicitly described and analyzed in terms of system outputs corresponding to the inputs of the plunge grinding conditions. The analysis discussed the influence of system stiffness on the time constant that governs the transient behaviors of process parameters such as forces, power, and machine deflection. Also, it clarified that system stiffness is composed of machine stiffness and wheel contact stiffness, and these stiffnesses significantly affect grinding performance indicators such as productivity and grinding accuracy.

The elastic deflection of the grinding wheel was accurately measured and a function for representing the deflection nature under various contact loads was derived. The function provides the non-linear contact stiffness with respect to the normal load. The contact stiffnesses of four kinds of grinding wheels with different grades and bond materials were presented, and changes in the contact stiffness after dressing were discussed.

Experimental tests for both cylindrical grinding and centerless grinding were carried out, and it was experimentally confirmed that the time constant at ramp infeed and spark-out is significantly prolonged by reducing the grinding force. It was verified that a simulation of the grinding tests using the proposed model can accurately predict critical parameters like forces, machine deflection, and system stiffness during plunge operations. Finally, this paper emphasized that it is vital to take the effect of wheel contact stiffness into consideration during the design of the plunge grinding cycle.

The study provides the following conclusions.

(1) The equivalent stiffness of the plunge grinding system is composed of machine stiffness and wheel contact stiffness. The contact stiffness greatly depends on the normal contact load. It is confirmed by the measurement of wheel deflection and the plunge grinding tests with various infeed rates.

(2) The contact deflection of the grinding wheel behaves like a non-linear spring representing a local contact deflection at lower load and a linear spring expressing the elasticity of the wheel body itself at a higher load. Formulas representing the wheel deflection behaviors are presented.

(3) The contact stiffness significantly affects the time constant T that governs the transient behaviors in ramp infeed and spark-out grinding.

(4) The time constant T is drastically prolonged with reduced normal grinding force due to the reduction of contact stiffness at lower contact loads. The grinding tests revealed that the time constant T significantly changes by 2–2.6 times.

(5) All measured Al_2O_3 wheels exhibit very low contact stiffness at a specific load less than 3 N/mm. At a higher load greater than 4 N/mm, contact stiffness reaches a constant.

(6) Plunge grinding tests applying both cylindrical grinding and centerless grinding methods with various infeed rates experimentally verified the effect of wheel contact stiffness on the time constant T.

(7) As guidelines for plunge grinding cycle, the ramp infeed grinding time should be set to at least five times T and at least three times T for spark-out grinding.

Conflicts of Interest: The authors declare no conflict of interest. F.H. is a founder of Advanced Finishing Technology Ltd., in which he holds shares. H.I. is a founder of Toba Engineering, in which he holds shares. The sponsors of both companies had no role in the design, collection, analysis, or interpretation of data, the writing of this article, or the decision to submit it for publication.

Nomenclature

s	Laplace operator	d_{eq}	Equivalent wheel diameter
$D_e(s)$	Deflection of machine in s-domain	d_s	Diameter of grinding wheel
$F_i(s)$	Actual infeed rate in s-domain	d_w	Diameter of workpiece
$F_n(s)$	Normal grinding force in s-domain	f_c	Cut-off frequency
$G(s)$	Transfer function in s-domain	f_i	Actual infeed rate
$I_f(\mathbf{s})$	Command infeed in s-domain	h_{eq}	Equivalent chip thickness
$Q_w(s)$	MRR in s-domain	k_a	Stiffness of wheel contact area
$Q_w{}'(s)$	SMRR in s-domain	$k_a{}'$	Specific stiffness of wheel contact area
$R_w(s)$	Actual infeed in s-domain	k_b	Stiffness of wheel body
A	Constant	$k_b{}'$	Specific stiffness of wheel body
F	Ratio of Fn to fi	k_c	Contact stiffness of grinding wheel
F_n	Normal grinding force	$k_c{}'$	Specific contact stiffness of grinding wheel
F_t	Tangential grinding force	k_{eq}	Equivalent system stiffness
$F_n{}'$	Specific normal grinding force	k_m	Machine stiffness of grinding system
$F_t{}'$	Specific tangential grinding force	k_{mi}	Stiffness of i-th. mechanical structure
GW	Grinding wheel	$\hat{k_m}$	Estimated machine stiffness
I_f	Command infeed	k_s	Stiffness of wheel support system
I_p	Constant infeed rate	k_w	Stiffness of work support system
L	Contact load	k_{w0}	Stiffness of workpiece itself
L'	Specific contact load	l_c	Contact length
MRR	Material removal rate	n	Degrees of freedom
P_g	Grinding power	r_w	Actual infeed
Q_w	Material removal rate	t	Time
$Q_w{}'$	Specific material removal rate	t_p	Plunge grinding time
RW	Regulating wheel	t_s	Time at end of grinding
S	Constant	u	Specific energy
SMR	Specific material removal	v_s	Grinding speed
SMRR	Specific material removal rate	δ	Deflection
T	Time constant	δ_a	Deflection of wheel contact area
T_c	Contact time constant	δ_b	Deflection of grinding wheel body
T_m	Machine time constant	δ_c	Contact deflection of grinding wheel
WP	Workpiece	δ_s	Deflection at flange of grinding wheel
b	Width of workpiece	δ_w	Deflection of workpiece
c	Grinding method parameter	η	Force ratio (Fn/Ft)
d_e	Deflection of grinding machine		

References

1. Hahn, R.S. The Effect of Wheel-Work Conformity in Precision Grinding. *Trans. ASME* **1955**, *77*, 1325–1329.
2. Peklenik, J. Ermittlung von Geometrschen und Physikalischen Kenngrößenfür die Grundlagenforschung des Schleifens. Ph.D. Dissertation, Aachen Technical University, Aachen, Germany, 1957.
3. Snoeys, R.; Wang, I.-C. Analysis of the Static and Dynamic Stiffness of the Grinding Surface. In Proceedings of the 9th International MTDR Conference, Manchester, UK; 1968; p. 1133.
4. Brown, R.H.; Saito, K.; Shaw, M.C. Local Elastic Deflections in Grinding. *CIRP Ann.* **1970**, *19*, 105–113.
5. Kumar, K.V.; Shaw, M.C. The Role of Wheel-Work Deflection in Grinding Operations. *J. Eng. Ind.* **1981**, *103*, 73–78. [CrossRef]
6. Krug, H.; Honcia, G. Die Elastische Verformung bei Schleifwerkzeugen. *Werkstattstech* **1964**, *54*, 53.
7. Nakayama, K.; Brecker, J.; Shaw, M.C. Grinding Wheel Elasticity. *J. Eng. Ind.* **1971**, *93*, 609–613. [CrossRef]
8. Nakayama, K. Elastic Deformation of Contact Zone in Grinding. *Bull. Jpn. Soc. Prec. Eng.* **1971**, *5*, 93.

9. Zhou, Z.; Van Lutterwelt, C. The Real Contact Length between Grinding Wheel and Workpiece—A New Concept and a New Measuring Method. *CIRP Ann.* **1992**, *41*, 387–391. [CrossRef]

10. Rowe, W.B.; Morgan, M.N.; Qi, H.S.; Zheng, H.W. The Effect of Deformation on the Contact Area in Grinding. *CIRP Ann.* **1993**, *42*, 409–412. [CrossRef]

11. Hucker, S.A.; Farris, T.N.; Chandrasekar, S. Estimation of Contact Stiffness for Grinding of Hardened Steel. In Proceedings of the 1993 ASME Winter Annual Meeting, New Orleans, LA, USA, 28 November–3 December 1993; pp. 191–198.

12. Yamada, T.; Lee, H.S.; Matsushita, H. A Study on the Contact Stiffness of Grinding Wheels. *Key Eng. Mater.* **2004**, *257*, 263–266. [CrossRef]

13. Yamada, T.; Morgan, M.N.; Lee, H.S.; Miura, K. Calculation of the Contact Stiffness of Grinding Wheel. *Adv. Mater. Res.* **2011**, *325*, 54–59. [CrossRef]

14. Papanikolaou, M.; Salonitis, K. Contact stiffness effects on nanoscale high-speed grinding: A molecular dynamics approach. *Appl. Surf. Sci.* **2019**, *493*, 212–224. [CrossRef]

15. Hahn, R.S. On the Theory of Regenerative Chatter in Precision Grinding Operations. *Trans. ASME* **1954**, *76*, 563.

16. Furukawa, Y.; Miyashita, M.; Shiozaki, S. Vibration analysis and work-rounding mechanism in centerless grinding. *Int. J. Mach. Tool Des. Res.* **1971**, *11*, 145–175. [CrossRef]

17. Gurney, J.P. An Analysis of Surface Wave Instability in Grinding. *J. Mech. Eng. Sci.* **1965**, *7*, 198–209. [CrossRef]

18. Thompson, R.A. The Character of Regenerative Chatter in Cylindrical Grinding. *J. Eng. Ind.* **1973**, *95*, 858–864. [CrossRef]

19. Inasaki, I.; Karpuschewski, B.; Lee, H.-S. Grinding Chatter—Origin and Suppression. *CIRP Ann.* **2001**, *50*, 515–534. [CrossRef]

20. Snoeys, R.; Brown, D. Dominating Parameters in Grinding Wheel and Workpiece Regenerative Chatter. *Proc. MTDR* **1969**, 325–348.

21. Inasaki, I. Regenerative Chatter in Grinding. *Proc. MTDR* **1977**, 423–429.

22. Miyashita, M.; Hashimoto, F.; Kanai, A. Diagram for Selecting Chatter Free Conditions of Centerless Grinding. *CIRP Ann.* **1982**, *31*, 221–223. [CrossRef]

23. Hashimoto, F.; Kanai, A.; Miyashita, M. Growing Mechanism of Chatter Vibrations in Grinding Processes and Chatter Stabilization Index of Grinding Wheel. *CIRP Ann.* **1984**, *33*, 259–263. [CrossRef]

24. King, R.I.; Hahn, R.S. *Handbook of Modern Grinding Technology*; Service Network Incorporated: Princeton, MA, USA, 1998; pp. 3–29.

25. Malkin, S.; Koren, Y. Optimal Infeed Control for Accelerated Spark-Out in Plunge Grinding. *J. Eng. Ind.* **1984**, *106*, 70–74. [CrossRef]

26. Chiu, N.; Malkin, S. Computer Simulation for Cylindrical Plunge Grinding. *CIRP Ann.* **1993**, *42*, 383–387. [CrossRef]

27. Hashimoto, F. The Design of an Infeed Cylindrical Grinding Cycle. *Inventions* **2020**, *5*, 46. [CrossRef]

28. Kanai, A.; Suzuki, N.; Toriumi, M.; Miyashita, M. The Development of the "Load Compensator" for Cylindrical Grinding Machines. *CIRP Ann.* **1976**, *25*, 313–318.

29. Hashimoto, F.; Kanai, A.; Miyashita, M. High Precision Trueing Method of Regulating Wheel and Effect on Grinding Accuracy. *CIRP Ann.* **1983**, *32*, 237–239. [CrossRef]

30. Hashimoto, F.; Yamaguchi, H.; Krajnik, P.; Wegner, K.; Chaudhari, R.; Hoffmeister, H.-W.; Kuster, F. Abrasive Fine-Finishing Technology. *CIRP Ann.* **2016**, *65*, 597–620. [CrossRef]

31. Snoeys, R.; Peters, J. The Significance of Chip Thickness in Grinding. *CIRP Ann.* **1974**, *23*, 227–237.